Improving the Egomotion Estimation by Correcting the Calibration Bias

Ivan Krešo and Siniša Šegvić

University of Zagreb Faculty of Electrical Engineering and Computing, Unska 3, 10000 Zagreb, Croatia

{ivan.kreso, sinisa.segvic}@fer.hr

Keywords: stereo vision, camera motion estimation, visual odometry, feature tracking, camera calibration, camera model bias, deformation field

Abstract: We present a novel approach for improving the accuracy of the egomotion recovered from rectified stereoscopic video. The main idea of the proposed approach is to correct the camera calibration by exploiting the known groundtruth motion. The correction is described by a discrete deformation field over a rectangular superpixel lattice covering the whole image. The deformation field is recovered by optimizing the reprojection error of point feature correspondences in neighboring stereo frames under the groundtruth motion. We evaluate the proposed approach by performing leave one out evaluation experiments on a collection of KITTI sequences with common calibration parameters, by comparing the accuracy of stereoscopic visual odometry with original and corrected calibration parameters. The results suggest a clear and significant advantage of the proposed approach. Our best algorithm outperforms all other approaches based on two-frame correspondences on the KITTI odometry benchmark.

1 INTRODUCTION

Egomotion estimation is a technique which recovers the camera displacement from image correspondences. The technique is important since it can provide useful initial solution for more involved structure and motion (SaM) estimation approaches, which perform partial or full 3D reconstruction of the scene (Vogel et al., 2014). These approaches are appealing due to many potential applications in robotic (e.g. autonomous navigation (Diosi et al., 2011)) and automotive systems (e.g. driver assistance (Nedevschi et al., 2013) and road safety inspection).

Visual odometry (Nistér et al., 2004) is an interesting special case of egomotion estimation, where we wish to recover the camera trajectory over extended navigation essays with predominantly forward motion. In this special case, complex techniques such as batch reconstruction (global bundle adjustment) or recognizing previously visited places (loop closing) are inapplicable due to huge computational complexity involved and/or real time requirements. Hence, the only remaining option is to recover partial camera displacements over short sequences of input frames and to build the overall trajectory by patching them one after another. The resulting techniques are necessarily prone to the accumulation of incremental error, just as the classical wheel odometry, and are hence collectively denoted as visual odometry.

Due to conceptual simplicity and better stability, the camera egomotion is usually recovered in calibrated camera setups. Camera calibration is the process of estimating the parameters of a camera model which approximates the image formation. When we have a calibrated camera, we can map every image pixel to a 3D ray emerging from the focal point of the camera and spreading out to the physical world. Most perspective cameras can be calibrated reasonably well by parametric models which extend the pinhole camera with radial and tangential distortion. However, there is no guarantee that this model has enough capacity to capture all possible distortions of real camera systems in enough detail, especially when high reconstruction accuracy is desired. For example, many popular calibration models assume that the distortion center coincides with the principal point (Zhang, 2000), while it has been shown that this does not hold in real cameras (Hartley and Kang, 2005). A good overview of the camera calibration techniques and different camera models is given in (Sturm et al., 2011).

In this paper, we propose a novel approach for correcting the calibration of a stereoscopic camera system. In our experiments we come to the conclusion that the reprojection error is not uniformly distributed across the stereo image pair and that there exists a regularity in the reprojection error bias. We hypothesize that this disturbance in the reprojection error distribution is caused by inaccurate calibration due to insufficient capacity of the assumed distortion model. We propose to alleviate the disturbance by a local camera model (Sturm et al., 2011) formulated as a deformation field over a rectangular superpixel lattice in the two images of stereo pair. The proposed camera model has many parameters and hence requires a large amount of training data. Thus we propose to learn the parameters of our deformation field by exploiting the groundtruth camera motion and point feature correspondences in neighboring frames. The two principal contributions of this paper are as follows:

- a statistical analysis of the reprojection error by utilizing the groundtruth motion (subsection 4.2);
- a technique for correcting the camera calibration by exploiting the groundtruth motion for learning the image deformation field (subsection 4.3).

The experimental results presented in Section 5 show that the proposed approach is able to significantly improve the accuracy of the recovered camera motion. Our best algorithm outperforms all other approaches based on two-frame correspondences on the KITTI odometry benchmark.

2 RELATED WORK

An increasing number of papers focusing on visual odometry is an evidence of the problem importance. A detailed overview of the field can be found in (Scaramuzza and Fraundorfer, 2011; Fraundorfer and Scaramuzza, 2012). Most recent implementations are based on the approach that was proposed in (Nistér et al., 2004). The main contribution of their approach is that they did not define the cost function as a solution to point alignment problem in 3D space like earlier researchers (Moravec, 1980; Moravec, 1981). Instead, they used the 3D-to-2D cost function which minimizes the alignment error in 2D image space popularly called the reprojection error. The advantage of defining the error in image space is that it avoids the problem of triangulation uncertainty on the depth axis where the error variance is much larger compared to other two axes.

Most of the recent work is focused on constraining the optimization with multi-frame feature correspondences to achieve better global consistency (Badino et al., 2013; Konolige and Agrawal, 2008), by experimenting with new feature detectors and descriptors (Konolige et al., 2007) or by doing a further research in feature tracking and outlier rejection techniques (Badino and Kanade, 2011; Howard, 2008). Despite the vast amount of research on visual odometry done so far, we did not stumble upon any work addressing the impact of calibration to the accuracy of the results nor approaches to improve the calibration by employing the groundtruth motion data. We have previously shown (Kreso et al., 2013) that the accuracy of the reconstructed motion significantly depends on the quality of the calibration target (A4 paper vs LCD monitor). Now we go a step further by proposing a method for correcting the calibration bias due to insufficient capacity of the camera model.

3 STEREOSOPIC VISUAL ODOMETRY

A typical visual odometry pipeline is illustrated in Figure 1. Acquired images are given to the feature tracking process where the features are detected and descriptors extracted. The descriptors are then used to find the correspondent features in temporal (two adjacent frames) and spatial (stereo left and right) domain. Temporal and stereo matching can be performed independently if we do not apply feature detector in right images, or jointly if we do. After the feature matching the correspondences typically contain outliers which are usually rejected by random sampling. Finally we can optimize an appropriate cost function to recover the camera motion. Note that the image acquisition block in Figure 1 also contains the image rectification procedure which depends on camera calibration.

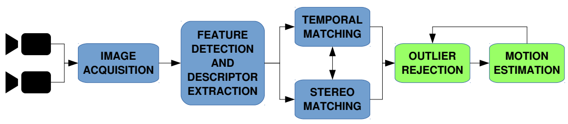

Figure 1: A typical visual odometry pipeline.

3.1 Feature Tracking

In order to recover the camera motion we must first find enough point correspondences between two stereo image pairs. It is assumed that the stereo rig is calibrated and that the images are rectified (their acquisition is described by a rectified stereo camera model). We use a similar tracking technique as (Nistér et al., 2004) and (Badino et al., 2013). We detect Harris point features (Harris and Stephens, 1988) only in left images and perform brute-force matching of their descriptors inside a search window to obtain left camera monocular tracks. To extract the descriptors we simply crop plain patches of size 15x15 pixels around each detected corner. We establish correspondences based on the normalized cross-correlation metric (NCC) between pairs of point features. In order to reduce the localization drift in tracking, we match all features in the current frame to the oldest occurrences.

To obtain the full stereo correspondences, we measure the disparity of every accepted left monocular track by searching for the best correspondence in the right image along the same horizontal row. Here again we compare the plain patch descriptors with NCC. Compared with matching of independently detected point features, this approach is more robust to poor repeatability at the price of somewhat larger computational complexity.

3.2 Cost Function Formulation

Let us denote an image point as $\mathbf{q} = (u,v)^\top$. Now we can define the points $\mathbf{q}^k_{i,t-1}$ in the previous frame $(t-1)$ and $\mathbf{q}^k_{i,t}$ in the current frame (t), where $i \in [1,N]$ is the index of the point and $k \in \{l,r\}$ is the value denoting if the point belongs to the left or right image. Let us subsequently denote $\mathbf{X}_{i,t}$ as the i-th 3D point in the current frame (t):

$$\mathbf{X}_{i,t} = (x,y,z)^\top = \boldsymbol{t}(\mathbf{q}^l_{i,t}, \mathbf{q}^r_{i,t}) \ , \qquad (1)$$

where $\boldsymbol{t}()$ is the function which triangulates the 3D point in world coordinate system from measured left and right image points. The goal of egomotion estimation is to recover the 3x3 rotation matrix $\mathbf{R}$ and the 3x1 translation vector $\mathbf{t}$ that satisfy the 6DOF rigid body motion of the tracked points.

In order to formulate the cost function we first need a camera model to describe the image acquisition process by connecting each image pixel with the corresponding real world light ray falling on the camera sensor. This can be done using perspective projection with addition of nonlinear lens distortion model. For brevity, we skip the modeling of lens distortion and stereo rectification and assume that the images are already rectified. The following equation introduces the pinhole camera model which uses the perspective projection π to project the world point $\mathbf{X} = (x,y,z)^\top$ to the point $\mathbf{q} = (u,v)^\top$ on the image plane.

$$\lambda \begin{pmatrix} u \\ v \\ 1 \end{pmatrix} = \pi(\mathbf{X},\mathbf{R},\mathbf{t}) = \begin{pmatrix} f & 0 & c_u \\ 0 & f & c_v \\ 0 & 0 & 1 \end{pmatrix} [\mathbf{R}|\mathbf{t}] \begin{pmatrix} x \\ y \\ z \\ 1 \end{pmatrix} \qquad (2)$$

The first part is the camera matrix containing the intrinsic camera parameters f, c_u and c_v. The distance of the focal point from the image plane f does not correspond directly to the focal length of the lens, since it also depends on the type and distance of the camera sensor. The principal point (c_u, c_v) is the image location where the z-axis intersects the image plane.

Now we can formulate the cost function for the two-frame egomotion estimation as a least squares optimization problem with the error defined in the image space:

$$\underset{\mathbf{R},\mathbf{t}}{\operatorname{argmin}} \sum_{i=1}^{N} \sum_{k}^{\{l,r\}} \|\mathbf{q}^k_{i,t} - \pi(\mathbf{X}_{i,t-1}, \mathbf{R}, \mathbf{t}_k)\|^2 \qquad (3)$$

$$\mathbf{t}_l = \mathbf{t}, \quad \mathbf{t}_r = \mathbf{t}_l - (b,0,0)^\top \qquad (4)$$

The cost function described by equation (3) is known as the reprojection error. To minimize the reprojection error, an iterative non-linear least squares optimization like first order Gauss-Newton (Geiger et al., 2011) or second order Newton method (Badino and Kanade, 2011) is usually employed. The equation (3) shows that we are searching for a motion transformation which will minimize the deviations between image points measured in the current frame and the reprojections of the transformed 3D points triangulated in the previous frame. The motion transformation is represented by the matrix $[\mathbf{R}|\mathbf{t}]$ which captures the motion of 3D points with respect to the static camera. We obtain the camera motion with respect to the world by simply taking the inverse transformation $[\mathbf{R}|\mathbf{t}]^{-1}$. One nice property of the transformation matrix emerging from the orthogonality of rotation matrices is that the inverse transformation is fast and easy to compute as shown in equation (5).

$$[\mathbf{R}|\mathbf{t}]^{-1} = \begin{pmatrix} \mathbf{R} & \mathbf{t} \\ \mathbf{0}^\top & 1 \end{pmatrix}^{-1} = \begin{pmatrix} \mathbf{R}^\top & -\mathbf{R}^\top\mathbf{t} \\ \mathbf{0}^\top & 1 \end{pmatrix} \qquad (5)$$

Note that the optimization is performed with respect to six free parameters, three describing the camera rotation matrix $\mathbf{R}$ and three describing the translation vector $\mathbf{t}$. The equation (4) describes the relationship between translations of the left and right cameras in the rectified stereo case. This is because the $\mathbf{X}_i$ is triangulated in coordinate system of the left camera and we need to shift it along x axis for the baseline distance b in the case when we are projecting to the right camera image plane. Note that the rotation matrix is the same for the left and right cameras because after the rectification they are aligned to have coplanar image planes and they share the same x-axis. Because the baseline b is estimated in the camera calibration and rectification steps the number of free parameters for translation remains three.

4 LEARNING AND CORRECTING THE CALIBRATION BIAS

In our previous research we have studied the influence of subpixel correspondence and online bundle adjustment to the accuracy of the camera motion estimated from rectified stereoscopic video. Our preliminary experiments have pointed out a clear advantage of these techniques in terms of translational and rotational accuracy on the artificial Tsukuba stereo dataset (Martull et al., 2012). However, to our surprise, this impact was significantly weaker on the KITTI dataset (Geiger et al., 2012; Geiger et al., 2013). Therefore, we have decided to investigate this effect by observing the reprojection error of two-frame point-feature correspondences under the KITTI groundtruth camera motion which was measured by an IMU-enabled GPS device.

4.1 Analysis of the Feature Correspondences

The analysis pointed out many perfect correspondences with large reprojection errors under the groundtruth camera motion. Figure 2 shows some examples of this effect where the points and the image patches describing them are displayed. If we look closely to any of the four patches, we can conclude that the localization error between any of the four frames should be less than 1 pixel. However, the reprojection errors evaluated for the groundtruth motion (cf. Table 1) are much larger than the localization errors (7 pixel vs 1 pixel). After observing this we wondered whether this is a property of a few outliers or whether there is a regularity with respect to the image location.

4.2 Statistical Analysis of the Reprojection Error

After observing many perfect correspondences with large reprojection errors we decided to verify whether this effect depends on image location. We divide the image space into a lattice of superpixel cells in which we accumulate the reprojection error vectors. Note that for every stereo correspondence containing 4 feature points we have two reprojection errors, one in the left image and the other in the right image. A single left or right reprojection error is defined by three feature points which can be observed in equation (3). Now for each reprojection error we share the responsibility between the three points equally, by dividing the vector by 3 and adding it to the cells containing the three points responsible for that error. Figure 3 shows the obtained distribution of the reprojection error vectors for left camera image in each cell. We computed the means of the error vector L2 norms and means and variances on the two image axes spanning the 2D error vector space. Additionally we used norm means to draw the heat map of the reprojection error distribution across the image.

By looking at the heat map and the means in Figure 3(c) we can conclude that the error minimum is close to the image center and that the error increases as we move away from the image center. Even more importantly, we can observe that the vector means given in Figure 3(d-e) are biased in certain directions and that this bias is significant considering the error variances given in Figure 3(f-g). Figure 3 shows that the minimal error of the camera model appears to be slightly displaced from the principal point of the image which is very close to the image center. This displacement may be showing us that the center of the radial distortion is not in the principal point of the camera as assumed by the employed rectification model. This problem was already observed in (Hartley and Kang, 2005) where the authors proposed a method for estimating the radial distortion center.

To confirm that these effects are not due to some strange bias within the tracker, we performed the same statistical analysis on the Tsukuba stereo dataset. Figure 4 shows the same heat map as we showed before. However, we see that here, on Tsukuba, the reprojection error is uniformly distributed without any observable pattern. Note that the contrast between cells is large due to histogram equalization but the actual values are distributed in the range from 0.16 to 0.18. Here we didn't show that the error vector means on u and v axes are zero, for brevity.

Table 1: Reprojection errors of the selected correspondences from Figure 2 evaluated for the groundtruth motion. The errors have much larger values than the uncertainty of the point feature locations, as seen in Figure 2.

Color	Left error	Right error
Red	7.10	7.01
Green	6.68	6.56
Blue	7.4	7.32
Yellow	6.75	6.35

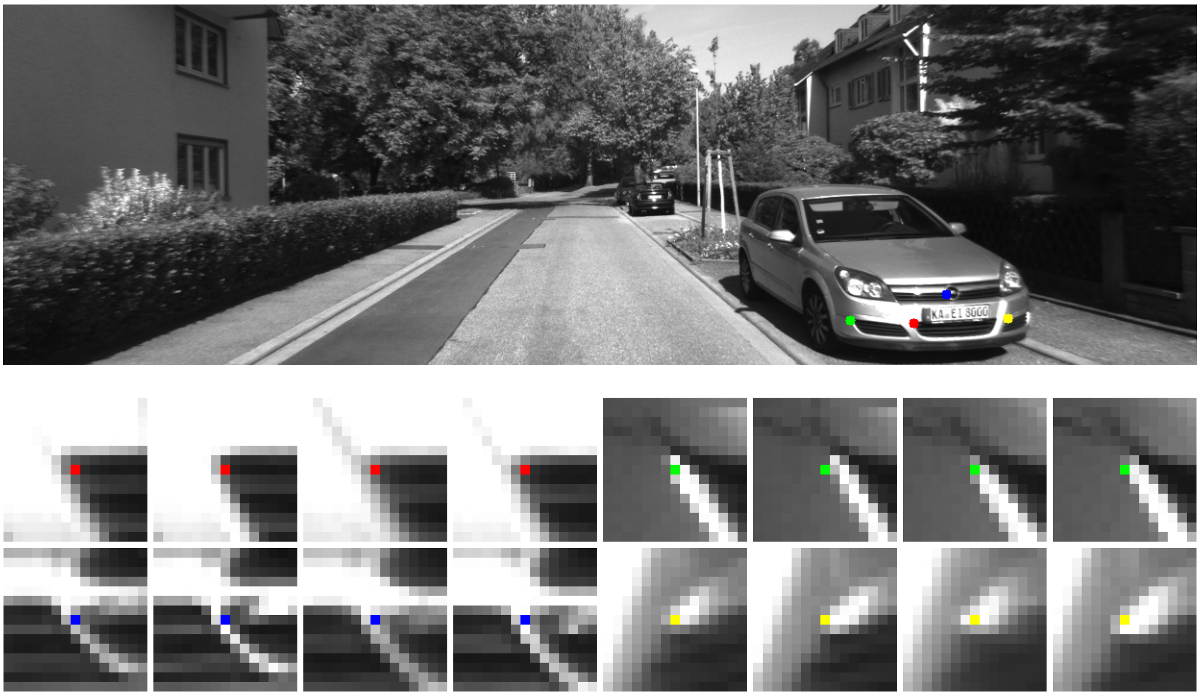

Figure 2: The image on the top corresponds to the frame #1 of the training KITTI sequence 03. Four point features have been annotated with different colors. The four bottom images show four 15x15 patches around each feature point in four different images (current-left, current-right, previous-left, previous-right). The localization error in the four images is less than 1 pixel. However, the reprojection errors evaluated for groundtruth motion are around 7 pixels as shown in Table 1.

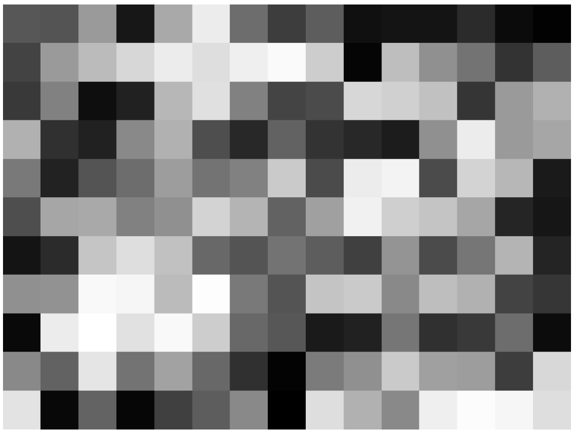

Figure 4: Heat map visualization of the distribution of reprojection error norms for the left camera image on the Tsukuba stereo dataset.

4.3 Learning the Stereoscopic Deformation Field

We hypothesize that the disturbance in the reprojection error distribution shown in Figure 3 is caused by inaccurate image rectification arising from the insufficient capacity of the underlying radial distortion model. Therefore, we devise a technique for correcting the camera calibration by exploiting groundtruth motion. After seeing that mean values of the vector errors deviate from zero and contain bias following some specific patterns we decided to try to learn the deformation field across discrete image cells. Each element of the deformation field contains two free parameters describing the translational shift on u and v image axes in the corresponding image cell. We differentiate between left and right camera and learn a separate deformation field for each of them. In order to define the cost function for learning the deformation field we denote $\mathbf{D}_u^l, \mathbf{D}_v^l, \mathbf{D}_u^r, \mathbf{D}_v^r$ as the deformation matrices for u and v axes and left and right cameras respectively. The motion parameters $\mathbf{R}_t$ and $\mathbf{t}_t$ in each frame t are taken from groundtruth data. Now if we define $\boldsymbol{d}()$ to be a simple function which takes an image point, determines to which cell of the image it belongs and uses a corresponding values from deformation matrices to apply the deformation, we can formulate the following optimization:

$$\underset{\mathbf{D}_u^l,\mathbf{D}_v^l,\mathbf{D}_u^r,\mathbf{D}_v^r}{\operatorname{argmin}} \sum_{t=1}^{M} \sum_{i=1}^{N} \sum_{k}^{\{l,r\}} \|\tilde{\mathbf{q}}_{i,t}^{k} - \pi(\mathbf{X}_{i,t-1}, \mathbf{R}_t, \mathbf{t}_{t,k})\|^2 \quad (6)$$

$$\tilde{\mathbf{q}} = \boldsymbol{d}(\mathbf{q}, \mathbf{D}_u, \mathbf{D}_v)$$

In order to optimize the deformation field loss

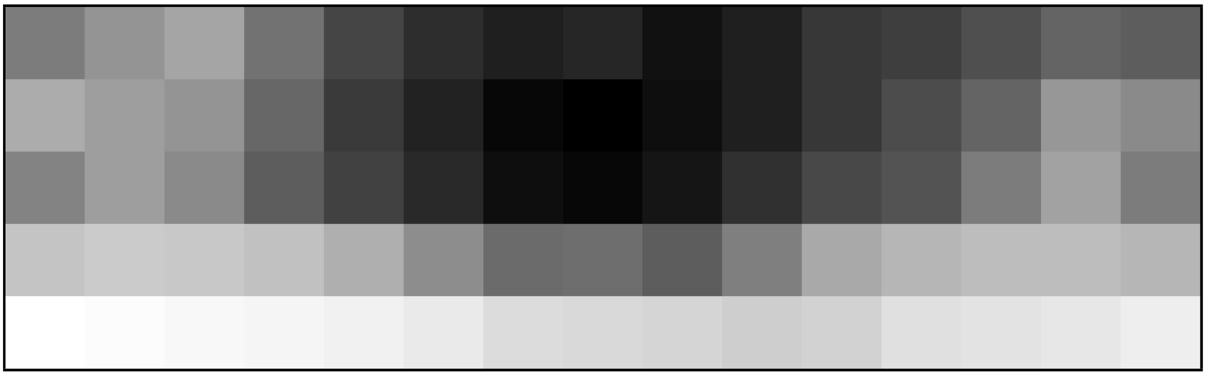

(a) Distribution of reprojection error vector norms in the left camera. Darker colors correspond to the lower values. The error increases in all directions from the minimum which is close to the image center.

16200	43960	60983	88632	159975	219012	167876	144061	171021	150130	100560	62776	39794	22913	8473
24992	79327	109810	141739	204386	315533	406393	384943	292353	216475	139156	98441	73760	45355	17461
27681	85761	122120	155581	216661	317709	424874	429657	290620	202883	141765	108101	86203	57941	22437
10618	46860	81195	115466	154868	174008	156019	131885	184310	155856	112752	80602	62472	44032	16037
1232	9360	18940	27301	38172	42210	38151	35922	40402	46551	41481	31306	26138	16588	5785

(b) Number of observed points in each cell.

0.35	0.367	0.374	0.344	0.301	0.277	0.267	0.272	0.262	0.267	0.292	0.295	0.314	0.334	0.332
0.383	0.369	0.367	0.337	0.293	0.27	0.249	0.245	0.254	0.267	0.292	0.308	0.334	0.367	0.36
0.359	0.369	0.36	0.333	0.297	0.274	0.254	0.249	0.263	0.283	0.305	0.326	0.349	0.373	0.35
0.417	0.439	0.436	0.411	0.386	0.363	0.342	0.343	0.333	0.352	0.381	0.395	0.398	0.398	0.394
0.606	0.587	0.581	0.573	0.538	0.508	0.477	0.474	0.465	0.455	0.462	0.483	0.492	0.494	0.518

(c) Reprojection error L2-norm means.

-0.129	-0.144	-0.171	-0.159	-0.118	-0.0729	-0.0487	-0.0328	-0.0125	-0.0196	-0.0245	-0.0176	-0.0328	-0.0658	-0.0713
-0.141	-0.124	-0.153	-0.132	-0.0902	-0.0489	-0.0238	-0.022	-0.0277	-0.0394	-0.053	-0.0626	-0.0824	-0.112	-0.125
-0.112	-0.116	-0.138	-0.115	-0.0814	-0.0509	-0.031	-0.0291	-0.0455	-0.0638	-0.0922	-0.0887	-0.109	-0.152	-0.144
-0.182	-0.188	-0.188	-0.168	-0.152	-0.0982	-0.0741	-0.0574	-0.0696	-0.0849	-0.115	-0.121	-0.116	-0.146	-0.134
-0.304	-0.255	-0.243	-0.234	-0.191	-0.131	-0.0874	-0.0892	-0.0945	-0.105	-0.108	-0.122	-0.116	-0.148	-0.18

(d) Reprojection error means on the u axis.

0.0173	0.0252	0.0219	0.0049	-0.00545	-0.00162	0.0048	0.00391	0.00424	0.0178	0.0288	0.0401	0.0601	0.0779	0.0624
0.0169	0.0372	0.0431	0.0345	0.0197	0.0146	0.00939	0.0117	0.0173	0.0265	0.0467	0.0613	0.0726	0.0801	0.0512
0.0255	0.05	0.0545	0.0499	0.0425	0.0345	0.0234	0.0204	0.0325	0.0407	0.0517	0.0581	0.07	0.069	0.0369
0.0641	0.0826	0.0884	0.0924	0.0891	0.0773	0.0769	0.065	0.0779	0.0842	0.0821	0.0921	0.0918	0.0811	0.053
0.144	0.131	0.131	0.148	0.126	0.141	0.128	0.128	0.121	0.133	0.149	0.156	0.166	0.175	0.15

(e) Reprojection error means on the v axis.

0.25	0.238	0.216	0.168	0.117	0.106	0.109	0.119	0.103	0.117	0.155	0.167	0.192	0.209	0.226
0.333	0.267	0.213	0.174	0.131	0.116	0.0947	0.0883	0.104	0.128	0.149	0.181	0.207	0.247	0.235
0.272	0.263	0.224	0.187	0.141	0.12	0.103	0.0968	0.116	0.144	0.169	0.218	0.243	0.243	0.23
0.352	0.347	0.336	0.291	0.228	0.218	0.205	0.237	0.193	0.213	0.27	0.294	0.319	0.296	0.306
0.567	0.543	0.555	0.509	0.452	0.42	0.424	0.437	0.416	0.374	0.386	0.416	0.418	0.382	0.448

(f) Reprojection error variances on the u axis.

0.118	0.131	0.138	0.125	0.123	0.131	0.128	0.13	0.136	0.126	0.135	0.125	0.115	0.11	0.0955
0.134	0.14	0.143	0.131	0.118	0.123	0.116	0.109	0.117	0.113	0.124	0.115	0.117	0.12	0.105
0.119	0.146	0.144	0.133	0.121	0.118	0.11	0.113	0.106	0.108	0.114	0.111	0.114	0.115	0.0932
0.129	0.16	0.167	0.158	0.17	0.169	0.145	0.143	0.14	0.152	0.164	0.151	0.132	0.124	0.116
0.258	0.258	0.25	0.262	0.299	0.289	0.23	0.232	0.243	0.213	0.206	0.227	0.231	0.207	0.193

(g) Reprojection error variances on the v axis.

Figure 3: Distribution of the reprojection error evaluated in groundtruth motion for sequence number 00 in KITTI dataset.

function, we collect the inlier tracks in all sequences by filtering them with groundtruth motion using a fixed error threshold. The collected tracks are serialized, saved to disk and later used by the optimization method which learns the stereoscopic deformation field. We minimize the cost function (6) using the Levenberg-Marquardt method which, in our experiments, converged faster than the line-search gradient descent methods to the same minimum. Note that the set of point features typically contains many outliers, since we only filter them with a permissive threshold on the reprojection error with respect to the groundtruth motion. This threshold has to be large enough in order to capture the impact of larger reprojection errors as we move further from the image center (cf. Figure 3). These outliers can exert a significant impact to the least-squares optimization. To take them into account we wrap the square loss into the robust Cauchy loss function given with the equation (7).

$$\rho(s) = a^2 log(1 + \frac{s}{a^2}) \tag{7}$$

Here the square loss output is denoted with s. By using the parameter a one can change the scale at which robustification takes place.

4.4 Integrating the Deformation Field in Motion Estimation

We will now integrate the learned stereoscopic deformation field into the expression (3) and define a new reprojection error cost function which applies the deformation field to all points before the optimization step. In order to achieve smooth deformation transitions, we compute the bilinear interpolation between the four cells of the deformation field which surround the point $\mathbf{x}_{i,t}^k$. In case when the bilinear interpolation is not possible we use linear interpolation (close to image edges) or we do not interpolate (close to image corners). Let us denote the interpolation function with $\boldsymbol{i}()$. Then the proposed cost function for recovering the camera motion can be formulated as follows:

$$\underset{\mathbf{R},\mathbf{t}}{\operatorname{argmin}} \sum_{i=1}^{N} \sum_{k}^{\{l,r\}} \|\hat{\mathbf{q}}_{i,t}^k - \pi(\mathbf{X}_{i,t-1}, \mathbf{R}, \mathbf{t}_k)\|^2 \tag{8}$$

$$\hat{\mathbf{q}} = \boldsymbol{i}(\mathbf{q}, \mathbf{D}_u, \mathbf{D}_v)$$

5 EXPERIMENTAL RESULTS

The KITTI odometry benchmark contains 11 training sequences with available groundtruth motion. These 11 sequences have been acquired with three different camera setups each of which has a distinct set of calibration parameters. We focus on the training sequences 04-10, which constitute the largest group of video sequences acquired with the same camera setup. Our experiments analyze the accuracy of the recovered camera motion according to the standard KITTI evaluation criteria (Geiger et al., 2013)[1]. We compare the performance of the proposed approach for correcting the calibration bias by a stereoscopic deformation field with two variants based on the libviso library[2]. All compared algorithms employ tracks extracted by our tracker described in Subsection 3.1. The tracker has been configured with the same set of parameters in all experiments.

5.1 Baseline and the feature weighting

The two libviso based variants differ in whether the procedure which we call feature weighting is applied or not. The simpler of these two variants (the one without feature weighting) shall be referred to as the baseline. Feature weighting can also be viewed as a way to improve the recovered camera motion by compensating inadequate calibration. This procedure weights the reprojection error residuals $\|\mathbf{q}_{i,t}^k - \pi(\mathbf{X}_{i,t-1}, \mathbf{R}, \mathbf{t}_k)\|^2$ and the corresponding Jacobians of the Gauss-Newton optimization according to the horizontal distance of $\mathbf{q}_{i,t}^k$ from the image origin. The libviso library determined these weights as follows:

$$w_i = \left(\frac{|u_i - c_u|}{|c_u|} + 0.05 \right)^{-1} \tag{9}$$

We did not find any explanation in the paper about libviso for how the equation (9) was chosen.

5.2 Leave One Out Evaluation

We test the impact of the proposed approach for correcting the camera calibration by a stereoscopic deformation field by leave-one-out evaluation on the training sequences 04-10. Therefore, we learn the stereoscopic deformation field ($\mathbf{D}_u^l, \mathbf{D}_v^l, \mathbf{D}_u^r, \mathbf{D}_v^r$) on six sequences and test its performance on the remaining sequence. This step is repeated seven times. The obtained results are presented in Tables 2 and 3. Please note that the columns labeled trans. show the relative translational error of the recovered motion in percents of the traveled distance, while the columns labeled rot. show the relative rotation error in degrees per meter. The tables show that the proposed approach

[1]A script for evaluating the accuracy is available at: http://kitti.is.tue.mpg.de/kitti/devkit_odometry.zip .

[2]The libviso library can be accessed at: http://www.cvlibs.net/software/libviso/ .

significantly improves the accuracy of the recovered camera motion both with respect to the baseline implementation and with respect to the feature weighting. in all of the seven experiments.

Table 2: Leave one out evaluation: baseline vs stereoscopic deformation field (DF).

KITTI		Baseline		With DF	
Seq.	length	trans.	rot.	trans.	rot.
04	394 m	1.14	0.0094	0.78	0.0068
05	2206 m	1.29	0.0095	0.43	0.0030
06	1233 m	1.30	0.0069	0.53	0.0047
07	695 m	2.02	0.0221	0.40	0.0034
08	3223 m	1.45	0.0087	1.02	0.0048
09	1705 m	1.51	0.0067	0.97	0.0050
10	920 m	0.80	0.0067	0.70	0.0040
All	10 376 m	1.386	0.0089	0.771	0.0043

Table 3: Leave one out evaluation: baseline vs feature weighting (FW).

KITTI		Baseline		With FW	
Seq.	length	trans.	rot.	trans.	rot.
04	394 m	1.14	0.0094	0.63	0.0027
05	2206 m	1.29	0.0095	0.70	0.0047
06	1233 m	1.30	0.0069	0.75	0.0041
07	695 m	2.02	0.0221	0.86	0.0083
08	3223 m	1.45	0.0087	1.10	0.0056
09	1705 m	1.51	0.0067	1.16	0.0041
10	920 m	0.80	0.0067	0.65	0.0042
All	10376 m	1.386	0.0089	0.933	0.0051

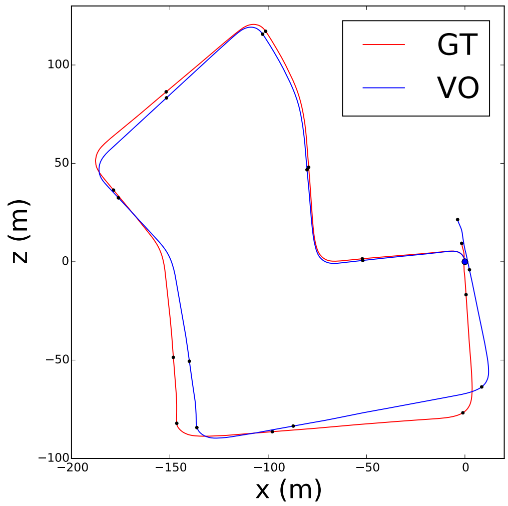

Figure 5: The reconstructed camera motion along the sequence 07 recovered without the stereoscopic deformation field and without the feature weighting (blue) is compared to the groundtruth camera motion (red).

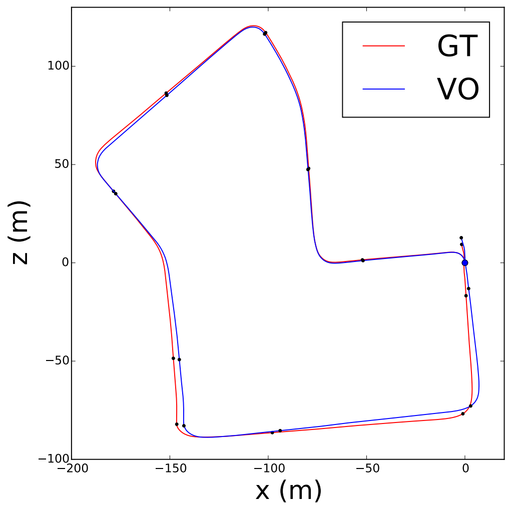

Figure 6: The reconstructed camera motion along the sequence 07 recovered with the feature weighting and without the stereoscopic deformation field (blue) is compared to the groundtruth camera motion (red).

5.3 Case study: the sequence 07

According to Table 2, the translational accuracy of the motion recovered by the baseline approach is 2.02%. Feature weighting improves that result to 0.86%. Finally, the stereoscopic deformation field further improves the accuracy to 0.40%. The 2D plots of the reconstructed three paths are compared to the groundtruth motion in Figures 5, 6 and 7.

5.4 Implementation

We have implemented all the described methods and experiments in C++. The OpenMP framework has been used to parallelize feature tracking and motion estimation. The implementation is based on the libviso library which was modified at several places in order to promote parallel execution and to support the track correction with the previously calibrated stereoscopic deformation field.

In all experiments the resolution of the deformation field was set to 21×69 bins in each of the two stereo images.

We implemented the optimization defined in expression (6) by using the Ceres Solver (Agarwal et al., 2014), an open source C++ library for modeling and

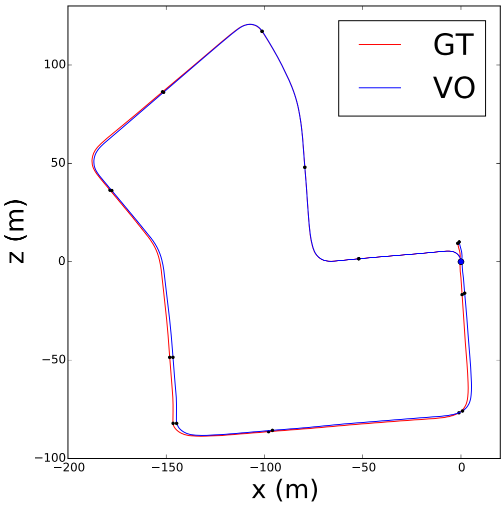

Figure 7: The reconstructed camera motion along the sequence 07 recovered with the stereoscopic deformation field and without the feature weighting (blue) is compared to the groundtruth camera motion (red).

solving large nonlinear least squares problem. One nice feature of the Ceres Solver is that it supports automatic differentiation if the cost function is written in the appropriate form.

6 CONCLUSION

Preliminary experiments in stereoscopic egomotion estimation had revealed that subpixel accuracy and multi-frame optimization have a substantially larger impact when applied to the artificial Tsukuba dataset than in the case of the KITTI dataset. We have decided to more closely investigate the peculiar KITTI results by observing the reprojection error of two-frame point-feature correspondences under groundtruth camera motion. The performed case-study analyses pointed out many near-to perfect correspondences with large reprojection errors. Additional experiments have shown that the means and the variances of the reprojection error significantly depend on the image coordinates of the three point features involved. In particular, we noticed that the reprojection error bias tends to be stronger as the point features become closer to the image borders. We have hypothesized that this disturbance is caused by inaccurate image calibration and rectification which could easily arise due to insufficient capacity of the underlying radial distortion model.

In order to test our hypothesis, we have designed a technique to calibrate a discrete stereoscopic deformation field above the two rectified image planes, which would be able to correct deviations of a real camera system from the radial distortion model. The devised technique performs a robust optimization of the reprojection error in validation videos under the known groundtruth motion. The calibrated deformation field has been employed to correct the feature locations used to estimate the camera motion in the test videos. We have compared the accuracy of the estimated motion with respect to the two baseline approaches operating on original point features. The experimental results confirmed the capability of the calibrated deformation field to improve the accuracy of the recovered camera motion in independent test videos, that is in videos which have not been seen during the estimation of the deformation field.

In our future work we would like to evaluate different regularization approaches in the loss function used to calibrate the stereoscopic deformation field. We also wish to evaluate the impact of the estimated correction of the calibration bias to the multi-frame bundle adjustment optimization.

ACKNOWLEDGEMENTS

This research has been partially supported by the European Union from the European Regional Development Fund by the project IPA2007/HR/16IPO/001-040514 ”VISTA - Computer Vision Innovations for Safe Traffic”.

Parts of this work have been performed in the frame of the Croatian Science Foundation project I-2433-2014.

REFERENCES

Agarwal, S., Mierle, K., and Others (2014). Ceres solver. `http://ceres-solver.org` .

Badino, H. and Kanade, T. (2011). A head-wearable short-baseline stereo system for the simultaneous estimation of structure and motion. In *IAPR Conference on Machine Vision Application*, pages 185–189.

Badino, H., Yamamoto, A., and Kanade, T. (2013). Visual odometry by multi-frame feature integration. In *First International Workshop on Computer Vision for Autonomous Driving at ICCV*.

Diosi, A., Segvic, S., Remazeilles, A., and Chaumette, F. (2011). Experimental evaluation of autonomous driving based on visual memory and image-based visual servoing. *IEEE Transactions on Intelligent Transportation Systems*, 12(3):870–883.

Fraundorfer, F. and Scaramuzza, D. (2012). Visual odometry: Part ii: Matching, robustness, optimization, and applications. *Robotics & Automation Magazine, IEEE*, 19(2):78–90.

Geiger, A., Lenz, P., Stiller, C., and Urtasun, R. (2013). Vision meets robotics: The kitti dataset. *International Journal of Robotics Research (IJRR)*.

Geiger, A., Lenz, P., and Urtasun, R. (2012). Are we ready for autonomous driving? the kitti vision benchmark suite. In *Conference on Computer Vision and Pattern Recognition (CVPR)*.

Geiger, A., Ziegler, J., and Stiller, C. (2011). Stereoscan: Dense 3d reconstruction in real-time. In *IV*. Karlsruhe Institute of Technology.

Harris, C. and Stephens, M. (1988). A combined corner and edge detector. In *Proceedings of the Alvey Vision Conference*, pages 147–152.

Hartley, R. I. and Kang, S. B. (2005). Parameter-free radial distortion correction with centre of distortion estimation. In *ICCV*, pages 1834–1841.

Howard, A. (2008). Real-time stereo visual odometry for autonomous ground vehicles. In *IROS*, pages 3946–3952.

Konolige, K. and Agrawal, M. (2008). Frameslam: From bundle adjustment to real-time visual mapping. *Robotics, IEEE Transactions on*, 24(5):1066–1077.

Konolige, K., Agrawal, M., and Solà, J. (2007). Large-scale visual odometry for rough terrain. In *ISRR*, pages 201–212.

Kreso, I., Sevrovic, M., and Segvic, S. (2013). A novel geo-referenced dataset for stereo visual odometry. *CoRR*, abs/1310.0310.

Martull, S., Peris, M., and Fukui, K. (2012). Realistic cg stereo image dataset with ground truth disparity maps. *Technical report of IEICE. PRMU*, 111(430):117–118.

Moravec, H. P. (1980). *Obstacle Avoidance and Navigation in the Real World by a Seeing Robot Rover*. PhD thesis, Stanford University.

Moravec, H. P. (1981). Rover visual obstacle avoidance. In *IJCAI*, pages 785–790.

Nedevschi, S., Popescu, V., Danescu, R., Marita, T., and Oniga, F. (2013). Accurate ego-vehicle global localization at intersections through alignment of visual data with digital map. *IEEE Transactions on Intelligent Transportation Systems*, 14(2):673–687.

Nistér, D., Naroditsky, O., and Bergen, J. R. (2004). Visual odometry. In *CVPR (1)*, pages 652–659.

Scaramuzza, D. and Fraundorfer, F. (2011). Visual odometry [tutorial]. *IEEE Robot. Automat. Mag.*, 18(4):80–92.

Sturm, P. F., Ramalingam, S., Tardif, J., Gasparini, S., and Barreto, J. (2011). Camera models and fundamental concepts used in geometric computer vision. *Foundations and Trends in Computer Graphics and Vision*, 6(1-2):1–183.

Vogel, C., Roth, S., and Schindler, K. (2014). View-consistent 3d scene flow estimation over multiple frames. In *ECCV*, pages 263–278.

Zhang, Z. (2000). A flexible new technique for camera calibration. *IEEE Trans. Pattern Anal. Mach. Intell.*, 22(11):1330–1334.